Chemical Engineering Journal 488 (2024) 150657

Contents lists available at ScienceDirect

Chemical Engineering Journal

journal homepage: www.elsevier.com/locate/cej

Controllable-gradient-porous cooling materials driven by multistage solvent displacement method

Yang Liu [a], Andrew Caratenuto [a], Fangqi Chen [a], Yi Zheng [a,b,*]

[a] Department of Mechanical and Industrial Engineering, Northeastern University, Boston, MA, 02115, USA
[b] Department of Chemical Engineering, Northeastern University, Boston, MA, 02115, USA

ARTICLE INFO

Keywords:
Radiative cooling
Gradient porous structure
Ultrahigh solar reflectance
Multistage solvent displacement
Ouzo effect

ABSTRACT

Passive radiative cooling holds significant potential for efficiently cooling terrestrial objects by simultaneously reflecting sunlight and radiating heat to the cold outer space. Numerous studies have designed high-performance radiative cooling structures using polymethyl methacrylate (PMMA) due to its inherent extinction coefficient. However, obtaining highly favorable spectral characteristics for reflecting sunlight using PMMA, often done through the fabrication of micro/nanoscale structures, remains a central barrier for widespread application. Herein, we report a facile, economical, and scalable multistage solvent displacement-based method for fabricating hierarchically gradient porous PMMA metafilms with highly efficient daytime and nighttime passive radiative cooling performance. Here, the "ouzo effect" works as the driving force for micro/nanopore formation by solvent displacement, which also controls the size of the pores based on different solution ratios. The PMMA metafilm features an ultrahigh solar reflectance of 0.99 and superior mid-infrared thermal emittance of 0.97, which allows for the average and peak subambient temperature drops of 4.6 °C and 8.2 °C, respectively, along with an average radiative cooling power of 90 W/m^2 during a 24-h uninterrupted thermal measurement. The hierarchically gradient micro/nanopore distribution of the PMMA metafilm significantly enhances the solar reflectance and thermal emittance within the atmospheric transparency window. Moreover, the multistage solvent displacement method is highly versatile and promising for fabricating porous structures, further offering a cost-efficient, eco-friendly, and sustainable manufacturing path for high-performance radiative cooling application.

1. Introduction

Cooling accounts for ~20% of global electricity consumption, and is particularly necessary in hot weather and climates, where air conditioning is essential for providing a comfortable and well-conditioned environment [1,2]. However, the increasing use of compressor-based cooling systems will substantially increase global energy consumption, significantly accelerating global warming and climate changes as a results [3,4]. Therefore, available energy-efficient and eco-friendly cooling technologies are receiving urgent attention in research and industry for terrestrial infrastructure cooling applications. The passive daytime radiative cooling (PDRC) strategy is a promising alternative cooling strategy which can help to slow or reverse global warming, as it achieves subambient cooling without requiring electricity or refrigerants [5,6]. PDRC applications are mainly enabled by spectrally selective materials, which simultaneously reflect sunlight (0.3–2.5 μm) and radiate infrared thermal radiation to the cold outer space (3 K) [7] through the atmospheric transparency window between 8 and 13 μm [8–14]. Accordingly, high solar reflectance (R_{solar}, λ ~ 0.3–2.5 μm) and high infrared thermal emittance (ε_{IR}, λ ~ 8–13 μm) are two crucial points for the design and fabrication of efficient PDRC materials and structures, as these properties help to maximize output power and minimize input power under direct sunlight [15–18].

Recently, a variety of energy-efficient PDRC structures and materials exhibiting high R_{solar} and high ε_{IR} have been proposed and fabricated, such as multilayer photonic structures [8,19–22], particle-distributed structures [23–27], porous structures [28–37], metamaterials [38–41], biomaterials [11,42] and bio-inspired materials [43–47]. In 2014, Raman and Fan et al. firstly designed PDRC multilayer structure, seven alternating dielectric layers of hafnium dioxide (HfO_2) and silicon dioxide (SiO_2) deposited on a silver substrate, which experimentally achieved a subambient temperature of 4.9 °C and a cooling power of

* Corresponding author at: Department of Mechanical and Industrial Engineering, Northeastern University, Boston, MA, 02115, USA.
E-mail address: y.zheng@northeastern.edu (Y. Zheng).

https://doi.org/10.1016/j.cej.2024.150657
Received 27 December 2023; Received in revised form 18 March 2024; Accepted 23 March 2024
Available online 29 March 2024

40.1 W/m^2 [8]. Another milestone PDRC structure fabricated by Yang and Yin et al. was glass-polymer hybrid metamaterial consisting of SiO_2 microspheres randomly distributed in the matrix polymethylpentene using a roll-to-roll method, which was able to reflect 96% of solar irradiation and processed a high infrared emissivity of 0.93 ($\lambda \sim 8$–13 μm), thereby achieving a cooling power of 93 W/m^2 under direct sunlight [9]. Mandal and Yang et al. experimentally realized ultrawhite poly(vinylidene fluoride-co-hexafluoropropene) coatings with micro- and nano-pores using a phase inversion-based method, which exhibited a solar reflectance of ~0.96 and an infrared emittance of ~0.97, resulting in a subambient cooling of 6 °C and an average cooling power of 96 W/m^2 during midday [48]. Recently, Wang et al. fabricated a hierarchically porous polymethyl methacrylate (PMMA) film with a close-packed micropore array and abundant random nanopores using a template method, which achieved a high solar reflectance of 0.95 and superior infrared thermal emittance of 0.98, and thereby realizing excellent subambient cooling performance [49]. Tian et al. synthesized an inorganic hydroxyapatite-based cooling paper with ultrahigh solar reflectance (0.99) and infrared emittance (0.9), which enabled cooling up to 5.1 °C below ambient temperature and yielded a cooling power of 104 W/m^2 under direct sunlight [38]. Nonetheless, achieving an optimal balance between structural designs and processing costs remains challenging for the majority of reported PDRC structures, which hinders impactful large-volume PDRC commercial applications. Therefore, a facile, cost-effective, and highly efficient PDRC approach is highly desirable for widespread practical radiative cooling applications.

Although the low-cost PMMA is widely used in radiative cooling because of its inherent extinction coefficient, the practical fabrication of micro/nanoscale structural characteristics for reflecting sunlight for practical applications remains a challenge. Here, we demonstrate a PMMA-based metafilm with hierarchically gradient internal micro/nanopores driven by a high-efficiency and low-cost multistage solvent displacement method. The as-obtained ultrawhite PMMA metafilm with gradient pore distribution (Fig. 1a) exhibits an excellent solar reflectance of 0.99 and noteworthy infrared thermal emittance of 0.97 within the atmospheric transparency window. This results in a superb PDRC performance, exemplified by the average and peak subambient temperature drops of 4.6 °C and 8.2 °C, respectively. Additionally, it maintains an average radiative cooling power of 90 W/m^2 during daytime a 24-h uninterrupted thermal measurement, obtained in conditions where the PMMA metafilm is directly exposed to sunlight and convective heat transfer without any wind cover. Both experimental data and theoretical calculation results verify that the hierarchically gradient micro/nanopore distribution in the PMMA metafilm significantly

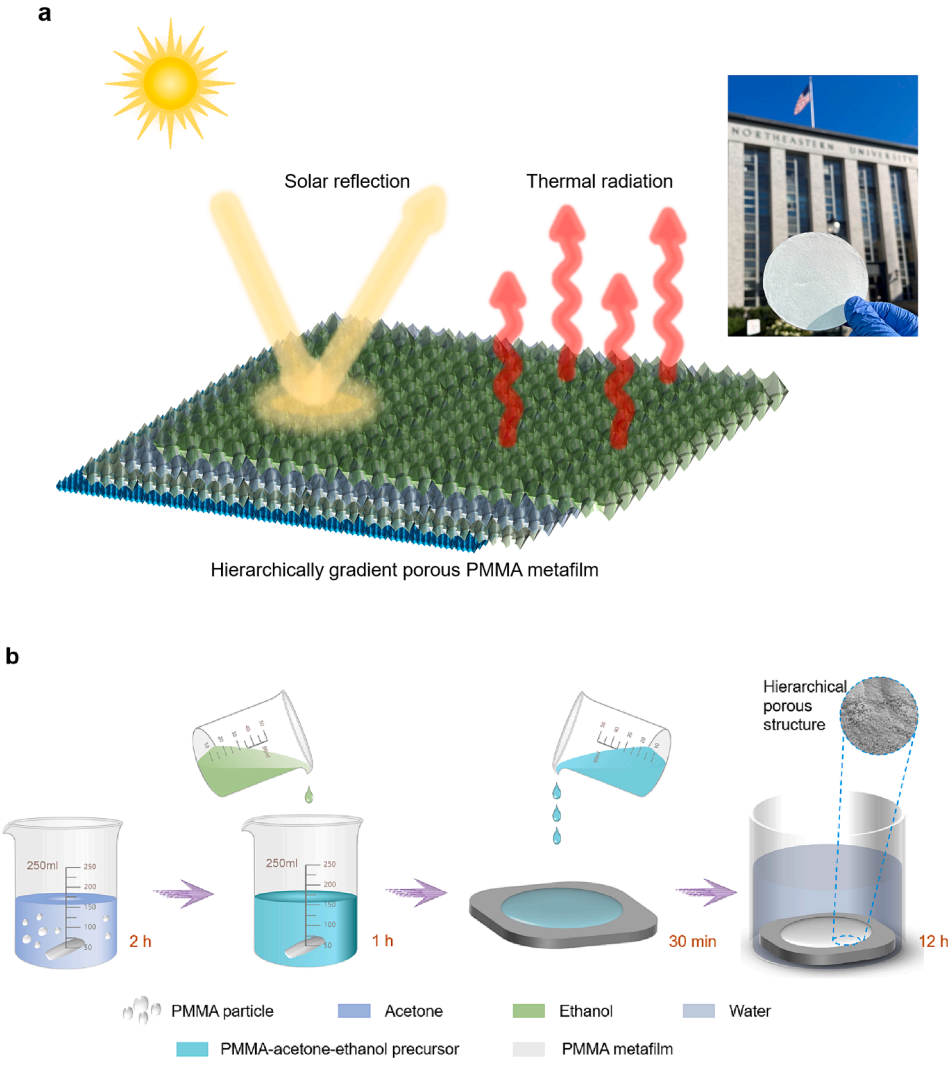

Fig. 1. Schematic illustrating the radiative cooling mechanism of the PMMA metafilm and its fabrication process. (a) Hierarchically gradient porous PMMA metafilm with high R_{solar} and ε_{ir} enables subambient cooling temperature under direct solar irradiance. (b) Schematic of the multistage solvent displacement-based process, showing the formation of a hierarchically gradient porous polymer from a solution of PMMA particles, acetone (solvent), ethanol (nonsolvent), and water (nonsolvent, pore-forming medium).

enhances its solar reflectance and thermal emittance. With these advantages, the gradient porous PMMA metafilm offers a superior material candidate for energy-efficient passive radiative cooling. Moreover, the multistage solvent displacement method is highly promising for fabricating porous radiative cooling structures at scale, which is essential for achieving widespread global sustainability benefits through high-volume applications.

2. Material and methods

2.1. Fabrication of PMMA metafilm with hierarchically gradient micro/nanopores

PMMA, molecular weight of ~120,000 from Sigma-Aldrich was first dissolved in acetone (Lab Alley), and then had ethanol (Lab Alley) added to produce a PMMA-acetone-ethanol precursor solution with a 1:2:2 mass ratio. The precursor solution was then drop-cast onto a smooth surface to achieve the desired thicknesses. Sufficient standing time of the precursor solution is essential to prevent irregular deformation of the sample due to the buoyancy of water in the following water immersion process. For a thickness of 1 mm, a 10 min standing time is used, and this standing time of precursor solution will increase with the thickness of the sample. After that, DI water was added to the container and submerged the PMMA sample for 12 hours. Finally, the PMMA sample was dried at 60 °C overnight.

2.2. Optical characterizations of the cooling structural polymers

The hemispherical spectral reflectance R (λ) and transmittance τ (λ) of PMMA sample were measured by a spectrophotometer (Jasco V770) in the ultraviolet, visible and near-infrared (0.3–2.5 μm) wavelength ranges. R (λ) and τ (λ) over the mid-infrared (2.5–20 μm) wavelength ranges were characterized using the FTIR spectrometer (Jasco 6600) equipped with a gold integrating sphere. The average values were calculated by six measurements at different sites of the PMMA sample. According to Kirchhoff's law, the spectral absorptivity α (λ) is equal to the spectral emissivity ε (λ) when an object in thermodynamic equilibrium; thus, α (λ) or ε (λ) can be calculated as ε (λ) = 1–R (λ)–τ (λ). The angular reflectance spectra of PMMA sample in the wavelength range of 0.3–18 μm at varying angles of incidence were measured by using standard wedge blocks of varying angles.

2.3. Theoretical model of the radiative cooling performance

When the PMMA metafilm is given access to a clear sky, its energy balance can be estimated by considering four heat transfer terms: absorbed incident solar radiation, absorbed atmospheric thermal radiation, heat transfer based on ambient conduction and convection, and the radiant output of the PMMA film. Using this model, the net cooling power P_{cool} of the PMMA metafilm can then be described as [8,10,17,50]:

$$P_{cool}(T) = P_{rad}(T) - P_{atm}(T_{amb}) - P_{solar} - P_{non\text{-}rad} \quad (1)$$

where T and T_{amb} are the surface temperature of the radiative cooler and the ambient temperature, respectively. Here, P_{rad}(T) is the radiative cooling power of the PMMA metafilm, and $P_{atm}(T_{amb})$ is the incident thermal radiation from the ambient absorbed by the structure. P_{solar} is the incident solar power absorbed by the structural PMMA film, and $P_{non\text{-}rad}$ is the non-radiative power due to ambient heat convection and conduction. Increasing solar reflectance (R_{solar}) and infrared thermal emissivity of the cooling structure will enhance the net cooling power defined in Eq. (1). P_{rad}(T) can be determined as follows:

$$P_{rad}(T) = A\int d\Omega\cos\theta\int_0^\infty d\lambda I_{BB}(T,\lambda)\varepsilon(\lambda,\theta) \quad (2)$$

where A is the surface area of the radiative cooler. Here, Ω is the solid angle, and θ denotes the angle between the direction of the solid angle and the normal direction of the surface. $I_{BB}(T,\lambda) = \frac{2hc^2}{\lambda^5}\frac{1}{e^{hc/(\lambda k_B T)}-1}$ is the spectral radiance of a blackbody. $\varepsilon(\lambda, \theta)$ is the directional emissivity of the surface at wavelength λ and angle θ.

The portion of the incident thermal radiation from atmosphere absorbed by radiative cooler $P_{atm}(T_{amb})$ is given by:

$$P_{atm}(T_{amb}) = A\int d\Omega\cos\theta\int_0^\infty d\lambda I_{BB}(T_{amb},\lambda)\varepsilon(\lambda,\theta)\varepsilon_{atm}(\lambda,\theta) \quad (3)$$

Here, the emissivity of the atmosphere is $\varepsilon_{atm}(\lambda,\theta) = 1 - t(\lambda)^{1/\cos\theta}$, where $t(\lambda)$ is the atmospheric transmission coefficient in the zenith direction. Solar irradiation absorbed by the radiative cooler P_{solar} can be calculated by:

$$P_{solar} = A\int_0^\infty d\lambda\varepsilon(\lambda,\theta_{solar})I_{AM1.5}(\lambda) \quad (4)$$

where $I_{AM1.5}$(λ) is the spectral irradiance intensity of solar irradiation at AM 1.5. In addition, the non-radiative heat transfer between the radiative cooler and the ambient environment can be determined as follows:

$$P_{non\text{-}rad}(T,T_{amb}) = Ah_c(T_{amb} - T) \quad (5)$$

In Eq. (5), $h_c = h_{cond} + h_{conv}$ is a nonradiative heat coefficient considering the heat conduction and convection ranging from 0 to 12 W/m^2/K.

The average hemispherical solar reflectance R_{solar} is a function of wavelengths and incident angles, which is defined as [51,52]:

$$R_{solar}(\lambda,\theta) = \frac{\int_{0.3\mu m}^{2.5\mu m} I_{solar}(\lambda)\bullet R(\lambda,\theta)d\lambda}{\int_{0.3\mu m}^{2.5\mu m} I_{solar}(\lambda)d\lambda} \quad (6)$$

Where λ is the wavelength of incident solar radiation over the range of 0.3–2.5 μm. $R(\lambda, \theta)$ is the surface's spectral directional reflectance.

The average hemispherical thermal emittance ε_{IR} within the atmospheric transmittance window is defined by [51]:

$$\varepsilon_{IR}(\lambda,\theta) = \frac{\int_{8\mu m}^{13\mu m} I_{BB}(\lambda)\bullet\varepsilon(\lambda,\theta)d\lambda}{\int_{8\mu m}^{13\mu m} I_{BB}(\lambda)d\lambda} \quad (7)$$

where $I_{BB}(\lambda)$ is the spectral radiation intensity by a blackbody based on Planck's law and $\varepsilon_{IR}(\lambda, \theta)$ is the surface's spectral directional thermal emittance over the range of 8–13 μm.

2.4. Thermal measurements of cooling temperature and cooling power tracking

PMMA metafilms and a wood sheet (control group) were placed inside a 100-Quart modified cooler box with a high thermal insulation, consisting of PS thermal insulation foam with thermal conductivity of 30 mW/m/K covered by a layer of reflective foil. The PMMA thin film with a diameter of 90 mm and a thickness of 1 mm was placed on a copper sheet (90 mm in diameter and thermal conductivity, 380 W/m/K) attached to the Kapton thin-film heater with a diameter of 90 mm in diameter and a thickness of 200 μm. T-type thermocouples were adhered the back of the PMMA metafilms to measure their real-time temperature. All thermocouples were connected to the National Instruments (NI) PXI-6289 multifunction I/O module to record temperature data during the test. The temperature tracking of the PMMA thin film to the ambient was performed by automatically switching the back-covered thin film heater on and off, controlled by a NI PXI-2586 relay module, which was driven by a NI LabVIEW program. The PID control algorithm controls the Kapton heater to intermittently heat PMMA film and maintains a temperature difference of less than 0.5 °C between the PMMA metafilm and ambient air during the experimental period. Here, the radiative cooling power from the PMMA film was equal to the

heating power generated by the electric heater. For comparison, the wood sheet (90 mm in diameter and 1.5 mm in thickness) was also adhered to the same copper sheet to measure its real-time temperature. As a control group, the wood sheet was also exposed to the sky while mounted in the same apparatus to compare the subambient cooling performances of PMMA metafilm. The outdoor radiative cooling experiment of PMMA film during both day and night were carried out on the rooftop of a four-story building at Northeastern University, Boston, MA, USA, 42.36◦ N, 71.06◦ W, May 31 - June 1, 2023).

3. Results and discussion

3.1. Fabrication and characterization of PMMA metafilm

Figure 1b illustrates the fabrication process of PMMA metafilm. Briefly, our multistage solvent displacement-based method for fabricating hierarchically gradient porous polymer begins with the preparation of a precursor solution of PMMA (polymer), acetone (solvent) and ethanol (nonsolvent). The precursor solution is then drop-cast onto the smooth surface to achieve the desired thicknesses. The solution is rested for dozens of minutes, depending on the area and thickness of the PMMA film, to prevent irregular deformation of the sample due to the buoyancy of water in the following water immersion process. The deposited PMMA-based film gradually generates gradient micro/nanopores within the cast thin film and finally solidifies during the immersion of DI water. A freestanding PMMA metafilm is obtained by peeling the film off the smooth surface. The joint effect of the rapid diffusion of acetone and ethanol in water and the hydrophobic PMMA separated from the water causes the gradient porous structure of PMMA metafilm. A 1 mm thick PMMA metafilm achieves a strong balance between high R_{solar}, ε_{IR}, and ductility. This thickness is treated as the default state of the PMMA metafilm in the following sections unless otherwise specified.

When structured by the solvent displacement-based technique, the PMMA film assembles into a hierarchical gradient porous structure, consisting of decreasing pore sizes from the bottom layer to the top layer, as seen in Fig. 2a-c. This structure simultaneously enables high R_{solar} and ε_{IR} when the bottom layer of the PMMA metafilm is faced towards the sun directly. Pore-size measurements indicate that the pore sizes of the bottom layer possess a broad distribution centered at ~1.0 μm (Fig. 2a), which can efficiently scatter the full spectrum of sunlight. Meanwhile, R_{solar} will be further improved by smaller nanopores with sizes below 1.0 μm, further enhancing the scattering of shorter and visible wavelengths (Fig. 2d-f). More SEM images of the cross-section view of the PMMA metafilm with gradient porous structure at different magnifications are presented in Supplementary Material (Fig. S1). Figure 3 demonstrates the hemispherical spectral reflectance and emissivity of a 1 mm thick PMMA metafilm displayed against the normalized AM 1.5 spectrum (ASTM G173), and the atmospheric transparency window. The PMMA metafilm placed backside up (the face with large pore size) with ~60% porosity exhibits an ultrahigh normalized solar reflectance $R_{solar} = 0.99$, which can strongly reflect sunlight regardless of the angle of incidence (0 - 60°) due to randomly distributed pores in the horizontal direction and gradually decreasing pore sizes in the vertical direction, thereby minimizing solar heat gain. Meanwhile, the PMMA metafilm also processes angle-independent and ultrahigh thermal emittance of 0.97 over the atmospheric transparency wavelengths (8–13 μm), thus ensuring massive heat loss based on infrared radiation to the cold outer space through the atmospheric window. One notable characteristic of the structural PMMA metafilm is that the hierarchical and gradient nano/micropores significantly decreases the mean scattering path and reduce transmission within the material, which further facilitates the scattering of ultraviolet-visible-near-infrared (UV-Vis-NIR) sunlight. Furthermore, PMMA-air void boundaries generate a distinct change in refractive index at the interfaces between the PMMA and air ($\Delta n = n_{PMMA} - n_{air} = 1.49 - 1 = 0.49$), which further contributes to the strong solar scattering.

PMMA is one of the commonly used polymers for passive radiative cooling due to its negligible extinction coefficient in the solar wavelength region and multiple extinction peaks from 8 to 13 μm [53], as shown in Fig. 4a. These two characteristics protect the PMMA film from heating under direct sunlight and significantly facilitate infrared radiative emission through the atmospheric transparency window, respectively, making the material intrinsically ideal for radiative cooling applications. Fourier transform infrared (FTIR) transmission spectra

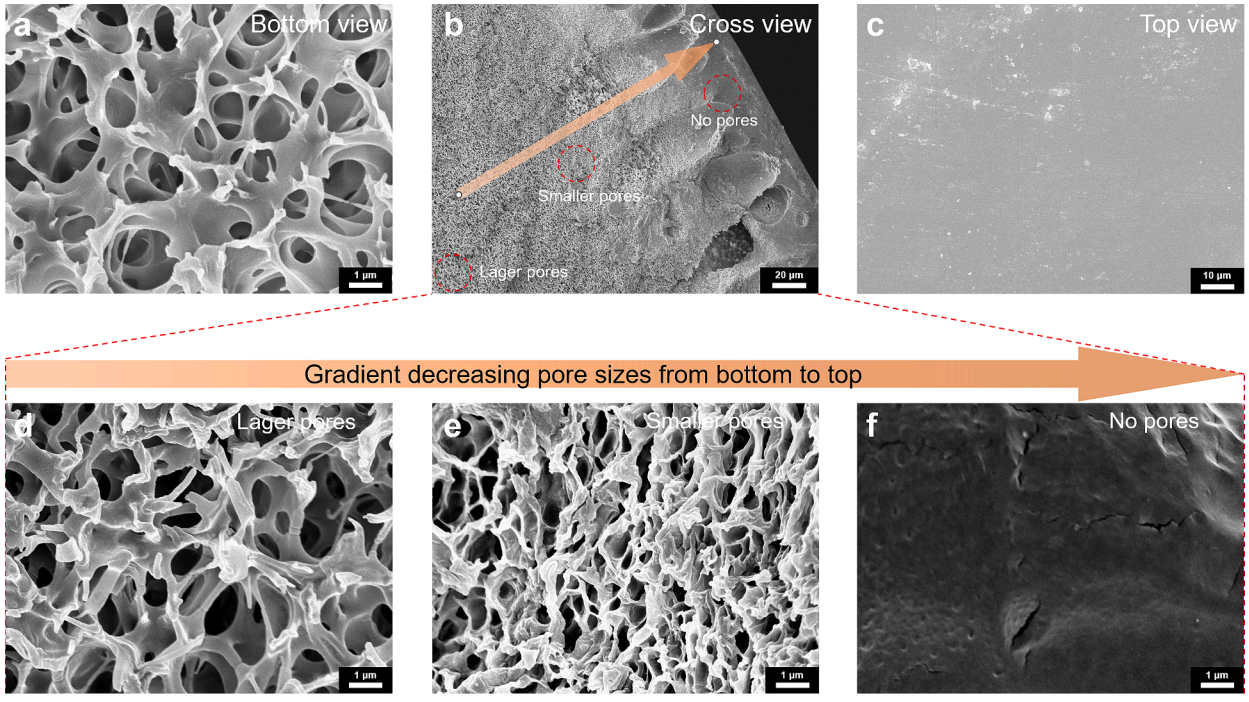

Fig. 2. Surface characterizations of PMMA metafilm. SEM micrographs of PMMA metafilm (a) bottom view, (b) cross-section view, and (c) top view. (d-f) Gradient decreasing pore distribution along the cross section of PMMA metafilm.

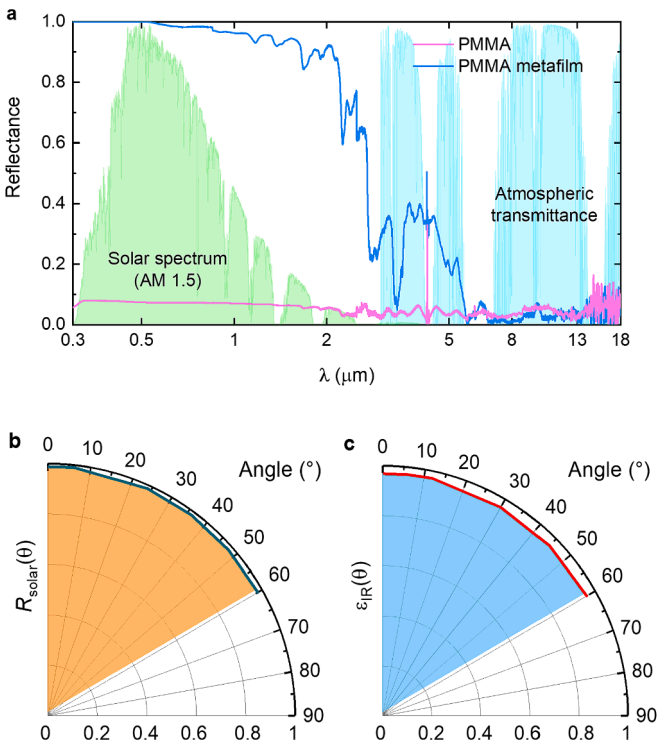

Fig. 3. (a) Hemispherical spectral reflectance of 1-mm-thick pristine PMMA film and PMMA metafilm plotted against the normalized AM 1.5 spectrum (ASTM G173) and the atmospheric transparency window, respectively. (b) High solar reflectance R_{solar} and (c) thermal emissivity ε_{IR} of PMMA metafilm at different angles of incidence.

show that PMMA exhibits strong emission bands between 8–13 μm, as seen in Fig. 4b, assigned to the stretching vibrations of C–O–C of the PMMA, showing that the infrared emission of PMMA naturally falls in the atmospheric transparency window. With these advanced characteristics good for PDRC application, our structural PMMA metafilm with ultrahigh R_{solar} and ε_{IR} can be able to achieve highly efficient passive daytime radiative cooling.

3.2. Size and distribution effects of porous structure on the optical properties of PMMA metafilm

To investigate the effect of adding ethanol (a nonsolvent of PMMA) into the precursor solution on the formation of the PMMA metafilm with micro/nanopores, we further compared the optical characteristics of PMMA-based films with different ethanol inputs (0 g, 5 g, 10 g, and 15 g, respectively) during the fabrication process. The precursor solution before adding ethanol consists of 5 g PMMA and 10 g acetone, as shown by the optical images in Fig. 5a-d. It is clearly seen that adding ethanol to the samples ($PMMA_{e5g}$, $PMMA_{e10g}$, and $PMMA_{e15g}$) provides a distinct white appearance after water immersion, which is absent from the sample where ethanol is omitted ($PMMA_{e0g}$), shown in Fig. 5a. Furthermore, Fig. 5e-h show the SEM images of the bottom layers of $PMMA_{e0g}$, $PMMA_{e5g}$, $PMMA_{e10g}$, and $PMMA_{e15g}$, respectively. Interestingly, the average pore size of these PMMA samples increases with the increasing proportion of ethanol in the PMMA-acetone-ethanol precursor solution, but no micro/nanopore formation (glitch-like structure) was seen in $PMMA_{e0g}$. For this reason, its solar reflectance suffers greatly, as the absence of pores significantly impedes scattering performance. Meanwhile, Fig. 6 compares their solar reflectance of the four PMMA films. The $PMMA_{e10g}$ presents the highest average solar reflectance R_{solar} = 0.99, while $PMMA_{e5g}$ and $PMMA_{e15g}$ drop gradually to lower average solar reflectance of 0.88 and 0.9, respectively. This is because their disordered pores are partially covered by excess PMMA for $PMMA_{5g}$ and their pore sizes are larger (~2 μm average diameter) for $PMMA_{10g}$, respectively, then suppressing scattering of the full range of sunlight effectively for $PMMA_{5g}$ and $PMMA_{10g}$. Figure 6b shows that all PMMA-based films exhibit strong thermal emittance in the atmospheric transparency window. Similarly, the thermal emissivity of the $PMMA_{e5g}$, $PMMA_{e10g}$, and $PMMA_{e15g}$ films rises in the range of mid-IR wavelengths compared with $PMMA_{e0g}$ films. This phenomenon can be attributed to the presence of hierarchically gradient micro/nanopore distributions in $PMMA_{e5g}$, $PMMA_{e10g}$, and $PMMA_{e15g}$ films, which provide smoother gradient transitions in refractive index across the interface between PMMA and air in comparison to $PMMA_{e0g}$ without a porous structure, resulting in the reduction in surface reflectance and then enhancing of thermal emissivity for these three films with ethanol involving in mid-IR wavelengths.

Figure 7 illustrates the mechanism of micro/nanopores formation in PMMA metafilm based on the multistage solvent displacement process. Here, the "ouzo effect" [54–57] works as the driving force for micro/nanopore formation by solvent displacement. Ouzo is an alcoholic beverage in Greece. Prior to consumption, it is customary to pour the clear liquor into a water-filled glass, causing it to swiftly transform into an opaque, milky-white solution, which results from the spontaneous aggregation (emulsification) of the water-insoluble solute trans-anethol. The ouzo effect has been extended to describe a general physical phenomenon that entails the spontaneous creation of metastable colloid

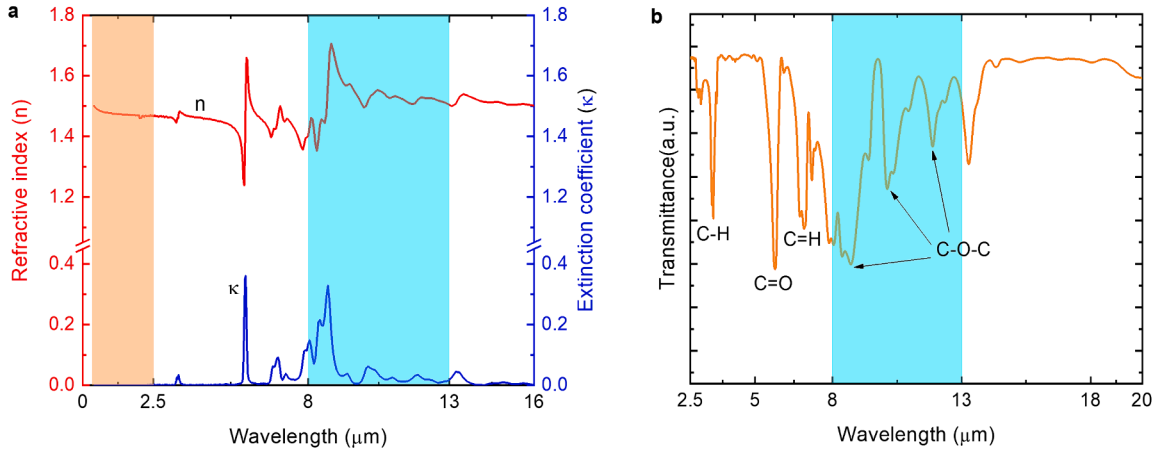

Fig. 4. Optical properties of PMMA. (a) Spectral refractive index (n) and extinction coefficient (κ) of PMMA. The extinction coefficient illustrates the negligible absorptivity of the material in the solar wavelength range (0.3–2.5 μm) and high emissivity with multiple extinction peaks between 8–13 μm. (b) FTIR transmittance spectrum of PMMA showing the C–O–C absorption bands within the atmospheric transparent window (8–13 μm).

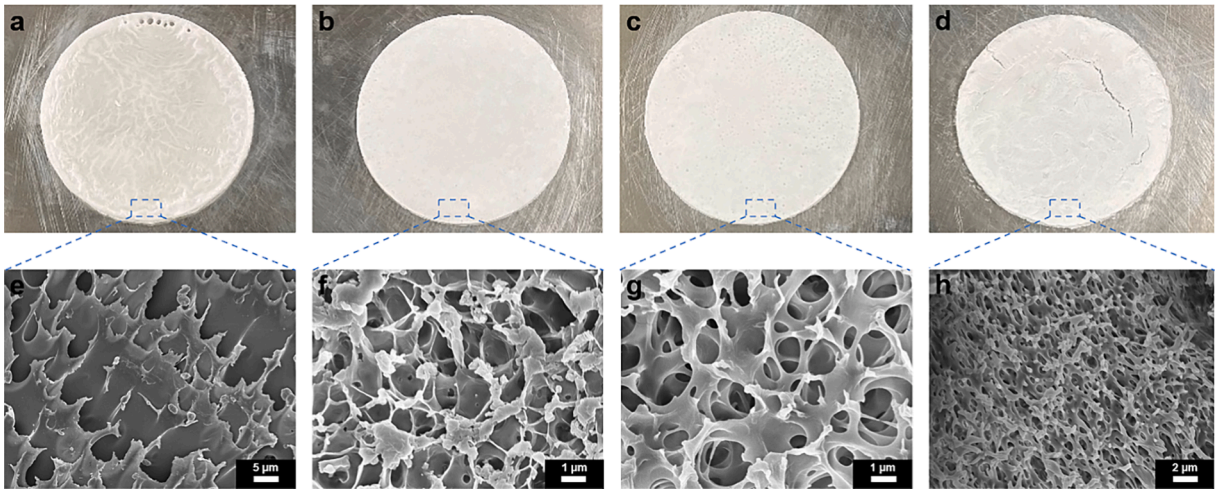

Fig. 5. Surface characterizations of PMMA-based films with different ethanol inputs (0 g, 5 g, 10 g, and 15 g, respectively). (a-d) Optical images and (e-h) SEM micrographs of the bottom layer of $PMMA_{e0g}$, $PMMA_{e5g}$, $PMMA_{e10g}$, and $PMMA_{e15g}$, respectively.

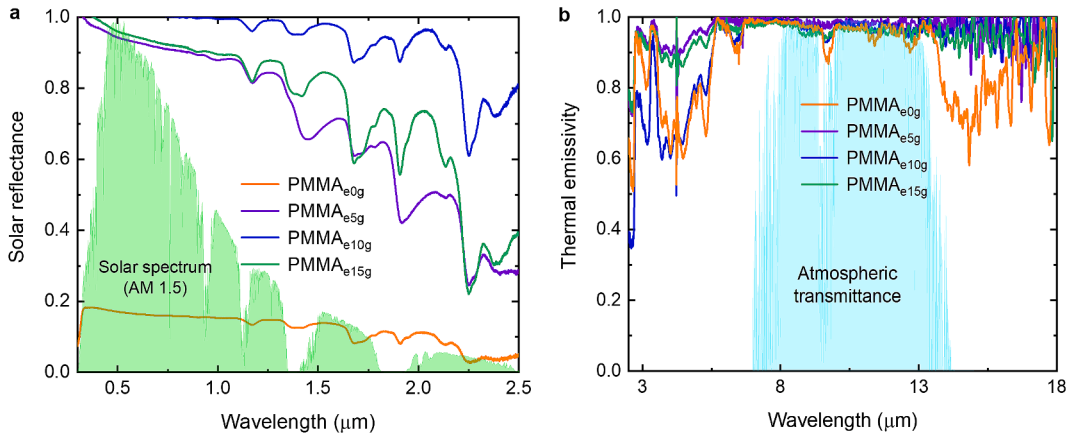

Fig. 6. Optical properties of different types of PMMA films. (a) Solar reflectance and (b) infrared thermal emissivity of $PMMA_{e0g}$, $PMMA_{e5g}$, $PMMA_{e10g}$, and $PMMA_{e15g}$ within the atmospheric transparency window.

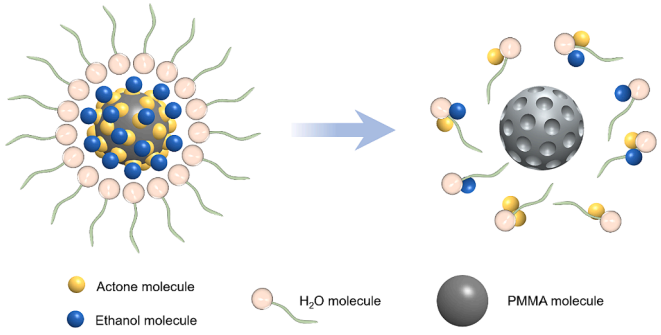

Fig. 7. Schematic presentation of micro/nanopores formation in PMMA metafilm driven by the "ouzo effect" in the process of the solvent displacement.

dispersions when water (acting as a nonsolvent) is mixed with a water-miscible solvent containing hydrophobic solutes. In the case of the PMMA metafilms, hydrophobic PMMA particles are dissolved in an acetone solvent. The concentration of acetone is then lowered by adding ethanol into the precursor solution, due to the insolubility of PMMA in ethanol and mutual dissolution of ethanol and acetone. Finally, the concentrations of acetone and ethanol both drop dramatically during the process of water immersion. Local supersaturation of hydrophobic PMMA molecules leads to spontaneous nucleation in the form of small structures that grow with time, resulting in the formation of abundant micro/nanopores in the PMMA metafilm. Here, the ethanol acts as a buffer during pore formation. Since PMMA particles are slowly soluble in acetone, it is hard for acetone to escape from the PMMA-acetone mixture quickly in the water immersion process if without adding ethanol, making it difficult to form micro/nanopores in PMMA film under the condition of maintaining the overall film structure without deformation, which is why $PMMA_{0g}$ has no micro/nanopores inside shown in Fig. 5e. However, the addition of ethanol in advance can reduce the binding force between PMMA and acetone, helping the acetone break away from PMMA quickly once immersed in water. Over time, this facilitates the subsequent pore formation with time in PMMA metafilm. Thus, ethanol is added to act as a buffer during pore formation.

The formation of hierarchically gradient micro/nanopores in the PMMA metafilm is primarily attributed to the adhesion force between the PMMA metafilm and the supporting substrate. During the initial stage of PMMA solidification in the water immersion process, the bottom surface of the PMMA-acetone-ethanol precursor solution establishes good contact with the supporting substrate and exhibits strong adhesion, primarily due to PMMA's inherent viscosity. Consequently, the bottom layer of the PMMA metafilm undergoes a stronger external traction force from the fixed-position substrate, thereby preventing the pores in the

lower layers driven by the solvent displacement from becoming smaller or being reduced by the penetration of the surrounding PMMA solution. However, the impact of the external traction force from the supporting substrate gradually weakens toward the upper layers of the PMMA metafilm. As solidification progresses in the PMMA, the pores forming in the upper layers may not fully develop and could gradually shrink in size or become filled by the surrounding PMMA solution. Therefore, throughout the solidification process of PMMA, the diminishing external traction force from bottom to top contributes to the hierarchically gradient micro/nanopores in the PMMA metafilm.

To further explore how the hierarchical gradient pores in the PMMA metafilm impact its solar reflectance, we compare decreasing (back side up) and increasing (front side up) pore size distributions of PMMA metafilm, as shown by the schematic diagrams in Fig. 8a,b, respectively. It is clearly seen that, compared with increasing pore size distribution of PMMA metafilm (front side up), more large micropores will participate in the reflection process of sunlight for PMMA metafilm with decreasing pore size distribution (back side up). But for the increasing pore size distribution, these disordered nanopores in the upper layers are too small to effectively scatter such longer wavelengths of solar light, and the sharply-changed gradient refractive index difference across the top PMMA-air boundary will cause a certain degree of reversed thermal reflection, resulting in a decrease in the long-wavelength reflectivity, as indicated by the red arrow in Fig. 8b. This is corroborated by the measured solar reflectance spectra in Fig. 8c. The solar reflectance of the PMMA's front side is significantly lower than that of the back side in longer wavelengths from 1.0 μm to 2.5 μm. Therefore, to achieve better cooling effect in the following outdoor cooling experiment, the PMMA metafilm is placed its backside facing the sun, as shown in Fig. 8a.

3.3. Passive radiative cooling performance of PMMA metafilm

The subambient radiative cooling performances of the hierarchically gradient porous PMMA metafilms were measured using a sample of diameter of 90 mm and a thickness of 1 mm. Measurements were taken from 6:00 PM on 31 May to 6:00 PM on 1 June 2023 using a 24-h uninterrupted thermal measurement on the rooftop of a four-story building at Northeastern University, Boston, MA. The inset of Fig. 9a schematically illustrates the structure inside the chamber. Further details about the experimental setup can be found in the experimental section. The temperature of the PMMA metafilm was measured in Chamber 1 with no input from the Kapton heater below. Simultaneously, the temperature of an identical PMMA metafilm was recorded in Chamber 2, in which the back-covered Kapton heater input was controlled by a proportional integral derivative (PID) control algorithm, maintaining the temperature of the PMMA metafilm at ambient temperature. This comparison allows for an accurate assessment of the cooling power during the test. As a control group, a commonly used balsa wood sheet [31] was chosen in Chamber 3 to further demonstrate the cooling ability of the PMMA - metafilm. The solar intensity, wind speed, and relative humidity over the experiment period was timely monitored by a commercial weather station, whose recorded data during the experimental period are seen in Fig. 9b,c. In addition, based on practical applications, no wind shields, such as infrared-transparent low-density polyethylene film, over the sample were used to reduce the convective heat transfer from ambient air. The temperature tracking curve, as seen in Fig. 9d, displays that the surface temperature of the PMMA metafilm follows the varying ambient temperature with a deviation of ±0.5 °C, demonstrating the reliability of the real-time measurement systems for the radiative cooling power of the PMMA metafilm. The temperature difference between the PMMA metafilm and the dew point during the experimental period is shown in Fig. S2. The PMMA metafilm has an average subambient temperature drop of 4.6 °C and an average radiative cooling power of 90 W/m^2 over a 24-h uninterrupted thermal measurement (Fig. 9e). During daytime, the PMMA metafilm exhibits a subambient temperature drop peak of 8.2 °C under a solar intensity of 780 W/m^2 and an average subambient temperature of 5.1 °C under a mean solar intensity of 833 W/m^2 from 12:00 PM to 2:00 PM (Fig. 9d). Meanwhile, the high-efficiency cooling effect of the PMMA metafilm decreases the PMMA film temperature below the ambient by 3.5° at the nighttime. As a comparison, the average temperature of wood sheet is about 8.0 °C higher than that of PMMA film during daytime, which also illustrates the excellent cooling capability of the PMMA thin film. The radiative cooling performance of the PMMA metafilm is comparable to that reported in previous studies (Supplementary Table S1).

We also examined the stability of the PMMA metafilms for outdoor application. The PMMA metafilm exhibits remarkable mechanical robustness, with an ultimate tensile strength of approximately 12.5 MPa

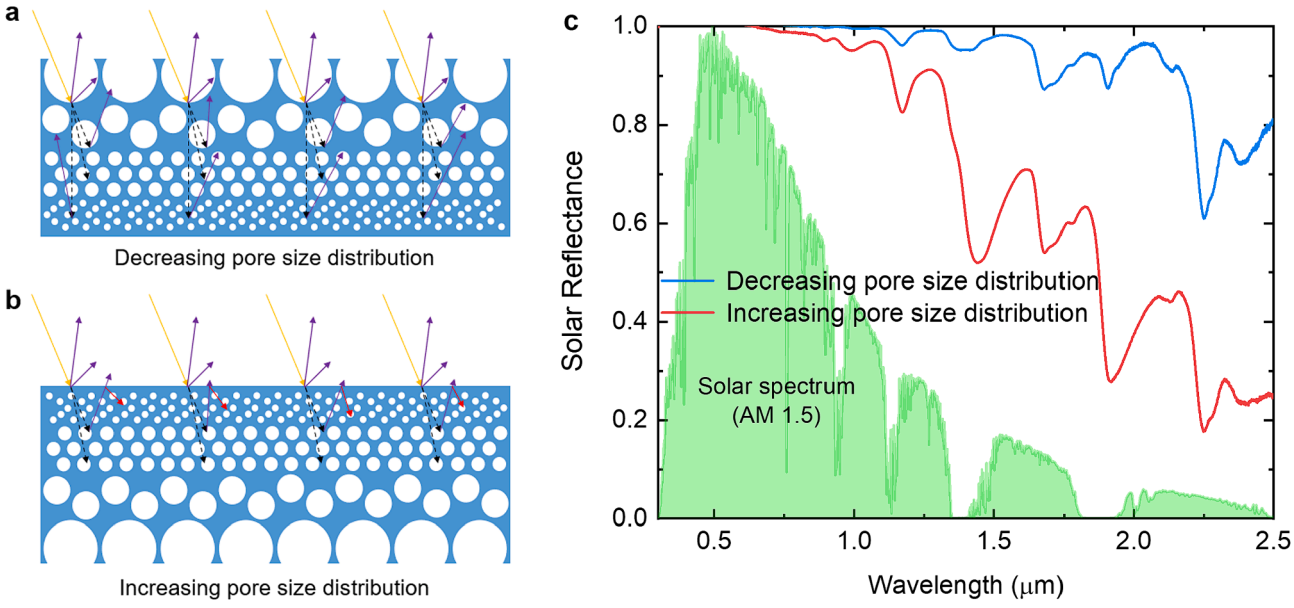

Fig. 8. Spectroscopic response of the gradient PMMA metafilm with different orientations. Schematic diagram showing the scattering mechanism of the PMMA metafilm with (a) decreasing (back side up) and (b) increasing (front side up) pore size distributions. (c) Solar reflectance of the decreasing and increasing pore size distributions of PMMA metafilm, respectively.

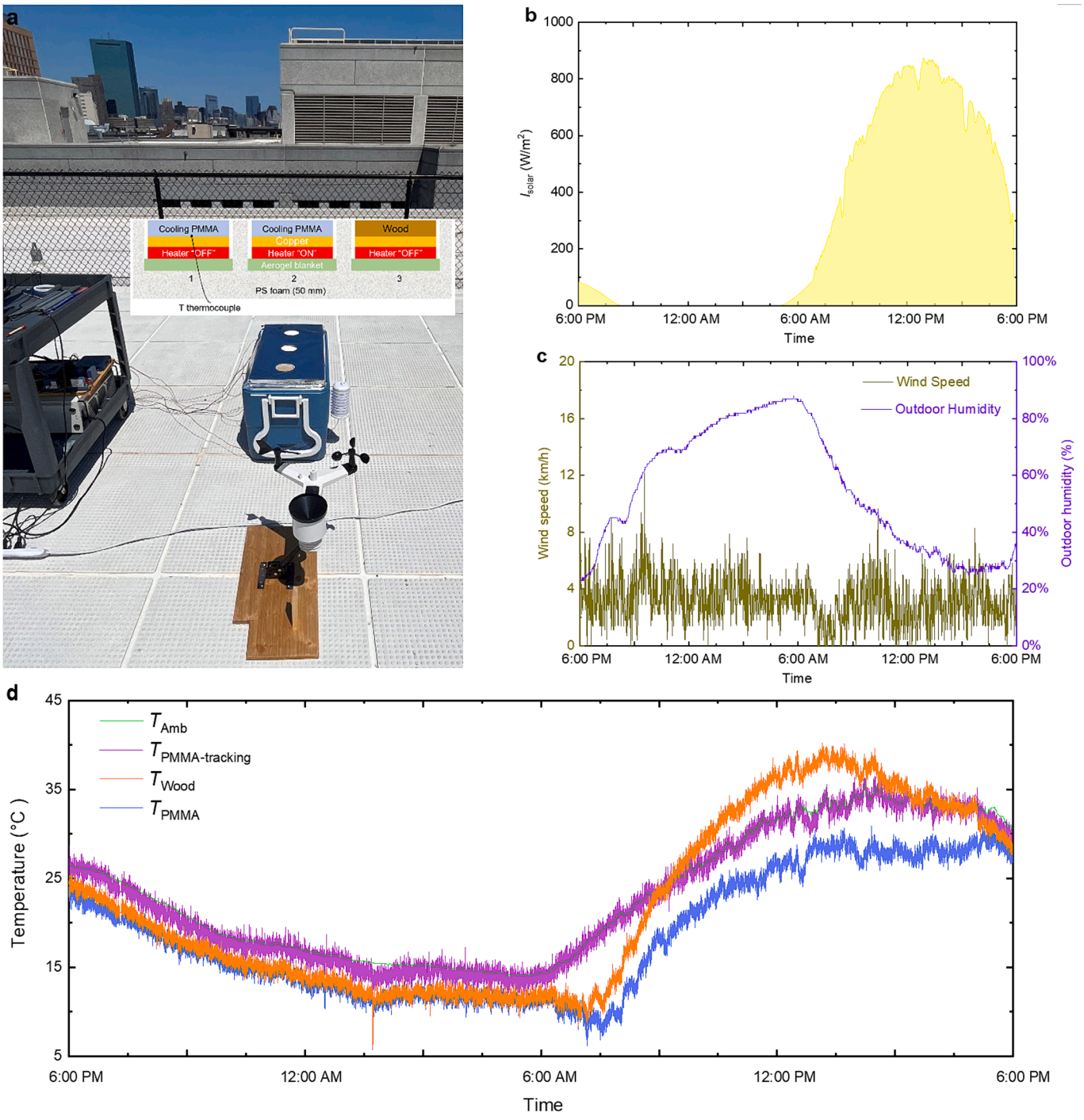

Fig. 9. Outdoor radiative cooling performance of the PMMA metafilm. (a) Schematic of the setup of real-time measurement for radiative cooling performance (Boston, MA, USA, 42.36° N, 71.06° W, May 31 - June 1, 2023). (b) Solar intensity, (c) wind speed, and relative humidity during the experimental period. (d) Temperature data for the ambient air, wood sheet, and PMMA metafilm during the experimental period. (e) The measured radiative cooling power of the PMMA metafilm.

(Fig. S3a). Moreover, a free-standing PMMA metafilm measuring 7 cm × 4.5 cm × 1 mm effortlessly bears a load exceeding 5 kg, indicating its suitability for engineering applications (Fig. S3b). And a test was conducted to assess the anti-fouling property of the PMMA metafilm in a simulated environment. Wet garden soil was applied to the PMMA metafilm, yet it failed to stain the surface. Subsequently, the soil was effortlessly washed away without causing any pollution, as depicted in Fig. S4. The washing process was captured using a phone camera, as illustrated in Supplementary Video S1. Besides, different harsh environmental tests, such as raindrop impact and UV exposure, did not cause any significant changes in the optical performance (Figs. S5, S6 and Supplementary Video S2). These tests demonstrate that the PMMA metafilm exhibits good stability under outdoor conditions, contributing to the preservation of its cooling performance in real-life applications.

Ambient heat convection can significantly affect the radiative cooling performance in practical applications, which is dependent on the ambient temperature and wind speed. Here, Fig. 10 presents the theoretical cooling power of the PMMA metafilm as a function of the PMMA

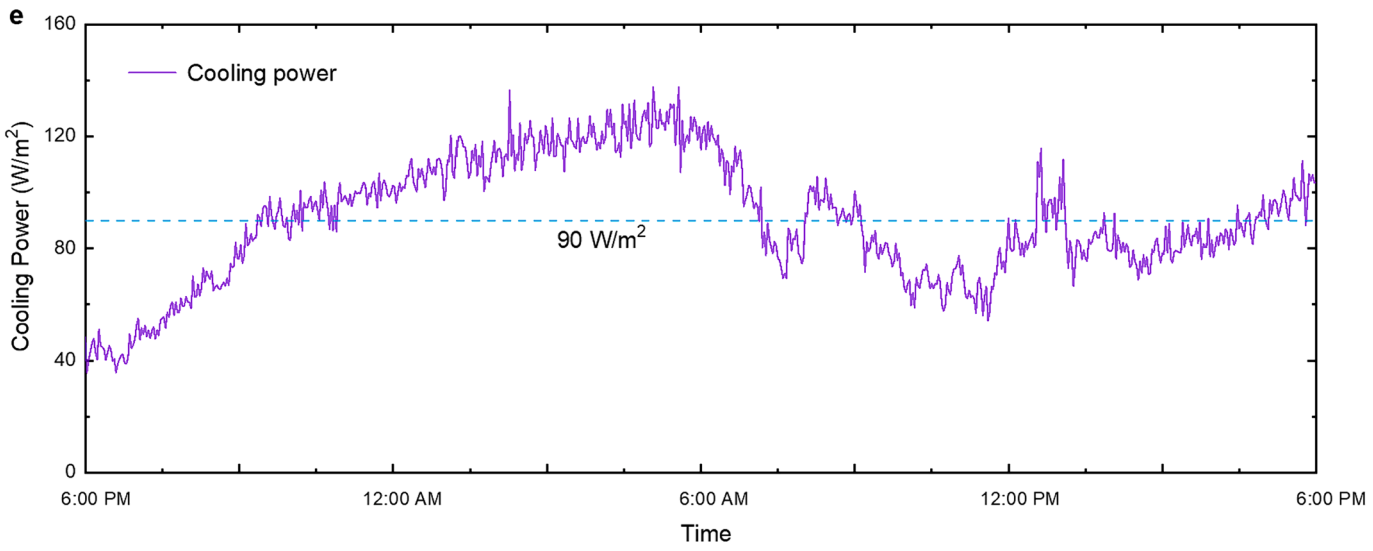

Fig. 9. (*continued*).

metafilm's temperature under different convection conditions during the nighttime and daytime, using the radiative cooling theoretical model, respectively. For these calculations, the ambient temperature T_{amb} is assumed to be 25 °C, and the solar radiation is fixed at 1000 W/m^2. With an increase of the PMMA metafilm temperature, the cooling power climbs until the temperature of the PMMA metafilm becomes equal to the ambient temperature, where the value of the non-radiative heat transfer term becomes zero based on Eq. (1) and (5). Various non-radiative heat transfer coefficients h_c of 0, 4, 8, and 12 W/m^2/K are considered in the cooling power calculation. A maximum net cooling power of 123.0 W/m^2 can be achieved during nighttime, while the cooling power maximum during the daytime is up to 91.8 W/m^2. The daytime maximum is lower than the calculated nighttime cooling power, due to the impact of the absorbed solar irradiance that neutralizes the part of the cooling power that the PMMA metafilm radiates out to the outer space during the daytime. Therefore, given that the actual cooling impact can be influenced by a range of factors, including atmospheric transmittance, water vapor content, inevitable experimental inaccuracies, and more, the obtained cooling data from our outdoor test remain justifiable and gratifying.

4. Conclusion

In conclusion, we have demonstrated and fabricated a hierarchically gradient porous PMMA metafilm for highly efficient subambient radiative cooling based on the multistage solvent displacement method, which can be easily-fabricated at scale for PDRC applications. The "ouzo effect" works as the driving force for micro/nanopore formation by solvent displacement and also controls the size of the pores based on different solution ratios. The obtained PMMA metafilm exhibits ultra-high solar reflectance over the broadband solar wavelength region - owing to the efficient backscattering occurring within its abundant, gradient micro/nanopores. It also has a high thermal infrared emissivity during the atmospheric transparency window based on the intrinsic molecular bond vibrations of PMMA. Both theoretical calculations and outdoor cooling measurements demonstrate the excellent subambient cooling performance of PMMA metafilm at the daytime and nighttime, even without convection shields to reduce ambient convection heat gain. This structural PMMA metafilm achieves an ultrahigh solar reflectance of 0.99 and a high mid-infrared emissivity of 0.97. These factors contribute to an average subambient temperature drop and an average radiative cooling power of 4.6 °C and 90 W/m^2, respectively, over a 24-h uninterrupted thermal measurement. During the daytime, a peak subambient temperature drop of 8.2 °C is achieved under a solar intensity of 780 W/m^2, along with an average subambient temperature drop of ~5.1 °C under a mean solar intensity of 833 W m^{-2} from 12:00 PM to 2:00 PM. Furthermore, the multistage solvent displacement method used to fabricate this PMMA metafilm offers a viable pathway for efficiently producing all-day passive subambient radiative cooling materials and structures, which can contribute to a substantial reduction

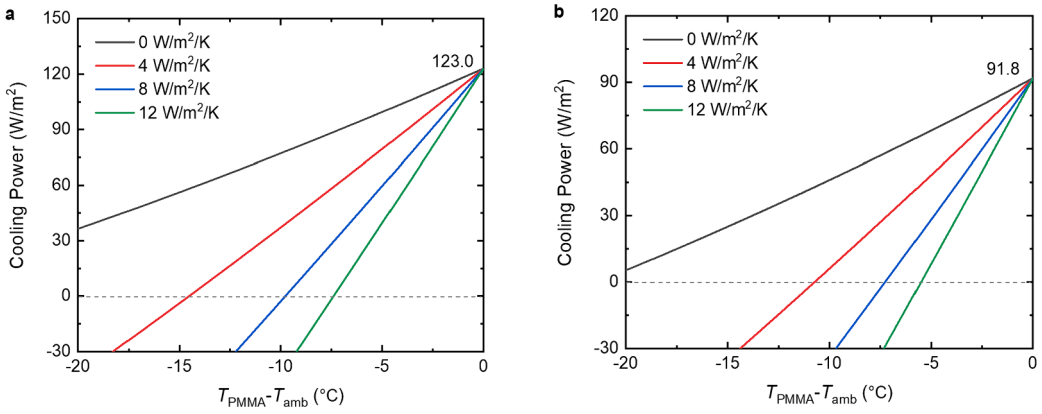

Fig. 10. Theoretical calculated net cooling power of PMMA metafilm. Calculated net cooling power during (a) the nighttime and (b) the daytime, respectively. h_c is the combined non-radiative heat transfer coefficient. Values of 0, 4, 8, and 12 for h_c are used in the calculations.

of energy consumption to help alleviate the growing crisis of global warming.

CRediT authorship contribution statement

Yang Liu: Writing – original draft, Visualization, Validation, Software, Resources, Methodology, Investigation, Formal analysis, Data curation, Conceptualization. **Andrew Caratenuto:** Visualization, Validation, Software, Methodology, Investigation, Formal analysis, Data curation. **Fangqi Chen:** Visualization, Validation, Software, Investigation, Data curation. **Yi Zheng:** Writing – review & editing, Visualization, Validation, Supervision, Project administration, Methodology, Investigation, Funding acquisition, Data curation, Conceptualization.

Declaration of competing interest

The authors declare that they have no known competing financial interests or personal relationships that could have appeared to influence the work reported in this paper.

Data availability

Data will be made available on request.

Acknowledgement

This project is supported by the National Science Foundation through grant number CBET-1941743 and PHY-1748958.

Appendix A. Supplementary data

Supplementary data to this article can be found online at https://doi.org/10.1016/j.cej.2024.150657.

References

[1] IEA. The Future of Cooling. https://www.iea.org/reports/the-future-of-cooling.
[2] M. Burke, S.M. Hsiang, E. Miguel, Global non-linear effect of temperature on economic production, Nature 527 (2015) 235–239.
[3] T.L. Frölicher, E.M. Fischer, N. Gruber, Marine heatwaves under global warming, Nature 560 (2018) 360–364.
[4] T.P. Hughes, J.T. Kerry, A.H. Baird, S.R. Connolly, A. Dietzel, C.M. Eakin, S. F. Heron, A.S. Hoey, M.O. Hoogenboom, G. Liu, Global warming transforms coral reef assemblages, Nature 556 (2018) 492–496.
[5] X. Zhang, Metamaterials for perpetual cooling at large scales, Science 355 (2017) 1023–1024.
[6] X. Yin, R. Yang, G. Tan, S. Fan, Terrestrial radiative cooling: Using the cold universe as a renewable and sustainable energy source, Science 370 (2020) 786–791.
[7] D. Fixsen, The temperature of the cosmic microwave background, ApJ 707 (2009) 916.
[8] A.P. Raman, M.A. Anoma, L. Zhu, E. Rephaeli, S. Fan, Passive radiative cooling below ambient air temperature under direct sunlight, Nature 515 (2014) 540–544.
[9] Y. Zhai, Y. Ma, S.N. David, D. Zhao, R. Lou, G. Tan, R. Yang, X. Yin, Scalable-manufactured randomized glass-polymer hybrid metamaterial for daytime radiative cooling, Science 355 (2017) 1062–1066.
[10] S. Fan, W. Li, Photonics and thermodynamics concepts in radiative cooling, Nat. Photon. 16 (2022) 182–190.
[11] T. Li, Y. Zhai, S. He, W. Gan, Z. Wei, M. Heidarinejad, D. Dalgo, R. Mi, X. Zhao, J. Song, A radiative cooling structural material, Science 364 (2019) 760–763.
[12] J. Chai, J. Fan, Solar and Thermal Radiation-Modulation Materials for Building Applications, Adv. Energy Mater. 13 (2023) 2202932.
[13] S. Zhang, Z. Wu, Z. Liu, Z. Hu, An Emerging Energy Technology: Self-Uninterrupted Electricity Power Harvesting from the Sun and Cold Space, Adv. Energy Mater. (2023) 2300260.
[14] K.-T. Lin, J. Han, K. Li, C. Guo, H. Lin, B. Jia, Radiative cooling: Fundamental physics, atmospheric influences, materials and structural engineering, applications and beyond, Nano Energy 80 (2021) 105517.
[15] X. Yu, J. Chan, C. Chen, Review of radiative cooling materials: Performance evaluation and design approaches, Nano Energy 88 (2021) 106259.
[16] D. Zhao, A. Aili, Y. Zhai, S. Xu, G. Tan, X. Yin, R. Yang, Radiative sky cooling: Fundamental principles, materials, and applications, Appl. Phys. Rev. 6 (2019) 021306.
[17] B. Zhao, M. Hu, X. Ao, N. Chen, G. Pei, Radiative cooling: A review of fundamentals, materials, applications, and prospects, Appl. Energy 236 (2019) 489–513.
[18] W. Xie, C. Xiao, Y. Sun, Y. Fan, B. Zhao, D. Zhang, T. Fan, H. Zhou, Flexible Photonic Radiative Cooling Films: Fundamentals, Fabrication and Applications, Adv. Funct. Mater. (2023) 2305734.
[19] Y. Liu, M. Antezza, Y. Zheng, Intelligent radiative thermostat induced by near-field radiative thermal diode, Mater. Today Phys. 27 (2022) 100828.
[20] Y. Liu, Y. Tian, X. Liu, F. Chen, A. Caratenuto, Y. Zheng, Intelligent regulation of VO2-PDMS-driven radiative cooling, Appl. Phys. Lett. 120 (2022) 171704.
[21] D. Chae, M. Kim, P.-H. Jung, S. Son, J. Seo, Y. Liu, B.J. Lee, H. Lee, Spectrally selective inorganic-based multilayer emitter for daytime radiative cooling, ACS Appl. Mater. Interfaces 12 (2020) 8073–8081.
[22] H. Ma, K. Yao, S. Dou, M. Xiao, M. Dai, L. Wang, H. Zhao, J. Zhao, Y. Li, Y. Zhan, Multilayered SiO2/Si3N4 photonic emitter to achieve high-performance all-day radiative cooling, Sol. Energy Mater. Sol. Cells 212 (2020) 110584.
[23] Y. Tian, H. Shao, X. Liu, F. Chen, Y. Li, C. Tang, Y. Zheng, Superhydrophobic and recyclable cellulose-fiber-based composites for high-efficiency passive radiative cooling, ACS Appl. Mater. Interfaces 13 (2021) 22521–22530.
[24] X. Li, J. Peoples, P. Yao, X. Ruan, Ultrawhite $BaSO_4$ paints and films for remarkable daytime subambient radiative cooling, ACS Appl. Mater. Interfaces 13 (2021) 21733–21739.
[25] X. Li, J. Peoples, Z. Huang, Z. Zhao, J. Qiu, X. Ruan, Full daytime sub-ambient radiative cooling in commercial-like paints with high figure of merit, Cell Rep. Phys. Sci. 1 (2020) 100221.
[26] X. Xue, M. Qiu, Y. Li, Q. Zhang, S. Li, Z. Yang, C. Feng, W. Zhang, J.G. Dai, D. Lei, Creating an eco-friendly building coating with smart subambient radiative cooling, Adv. Mater. 32 (2020) 1906751.
[27] P. Li, A. Wang, J. Fan, Q. Kang, P. Jiang, H. Bao, X. Huang, Thermo-optically designed scalable photonic films with high thermal conductivity for subambient and above-ambient radiative cooling, Adv. Funct. Mater. 32 (2022) 2109542.
[28] D. Li, X. Liu, W. Li, Z. Lin, B. Zhu, Z. Li, J. Li, B. Li, S. Fan, J. Xie, Scalable and hierarchically designed polymer film as a selective thermal emitter for high-performance all-day radiative cooling, Nat. Nanotechnol. 16 (2021) 153–158.
[29] A. Leroy, B. Bhatia, C.C. Kelsall, A. Castillejo-Cuberos, M. Di Capua, H.L. Zhao, L. Zhang, A. Guzman, E. Wang, High-performance subambient radiative cooling enabled by optically selective and thermally insulating polyethylene aerogel, Sci. Adv. 5 (2019) eaat9480.
[30] P. Yao, Z. Chen, T. Liu, X. Liao, Z. Yang, J. Li, Y. Jiang, N. Xu, W. Li, B. Zhu, Spider-Silk-Inspired Nanocomposite Polymers for Durable Daytime Radiative Cooling, Adv. Mater. 34 (2022) 2208236.
[31] Y. Liu, X. Liu, F. Chen, Y. Tian, A. Caratenuto, Y. Zheng, Oil-paper-umbrella-inspired passive radiative cooling using recycled packaging foam, J. Mater. Chem. A 11 (2023) 9152–9159.
[32] X. Wang, X. Liu, Z. Li, H. Zhang, Z. Yang, H. Zhou, T. Fan, Scalable flexible hybrid membranes with photonic structures for daytime radiative cooling, Adv. Funct. Mater. 30 (2020) 1907562.
[33] H. Yuan, R. Liu, S. Cheng, W. Li, M. Ma, K. Huang, J. Li, Y. Cheng, K. Wang, Y. Yang, Scalable Fabrication of Dual-Function Fabric for Zero-Energy Thermal Environmental Management through Multiband, Synergistic, and Asymmetric Optical Modulations, Adv. Mater. 2209897 (2023).
[34] W. Gao, Z. Lei, K. Wu, Y. Chen, Reconfigurable and renewable nano-micro-structured plastics for radiative cooling, Adv. Funct. Mater. 31 (2021) 2100535.
[35] J. Liu, H. Tang, C. Jiang, S. Wu, L. Ye, D. Zhao, Z. Zhou, Micro-Nano Porous Structure for Efficient Daytime Radiative Sky Cooling, Adv. Funct. Mater. 32 (2022) 2206962.
[36] B. Xiang, R. Zhang, Y. Luo, S. Zhang, L. Xu, H. Min, S. Tang, X. Meng, 3D porous polymer film with designed pore architecture and auto-deposited SiO2 for highly efficient passive radiative cooling, Nano Energy 81 (2021) 105600.
[37] C. Feng, P. Yang, H. Liu, M. Mao, Y. Liu, T. Xue, J. Fu, T. Cheng, X. Hu, H.J. Fan, Bilayer porous polymer for efficient passive building cooling, Nano Energy 85 (2021) 105971.
[38] Y. Tian, X. Liu, Z. Wang, J. Li, Y. Mu, S. Zhou, F. Chen, M.L. Minus, G. Xiao, Y. Zheng, Subambient daytime cooling enabled by hierarchically architected all-inorganic metapaper with enhanced thermal dissipation, Nano Energy 96 (2022) 107085.
[39] S.-Y. Heo, G.J. Lee, D.H. Kim, Y.J. Kim, S. Ishii, M.S. Kim, T.J. Seok, B.J. Lee, H. Lee, Y.M. Song, A Janus emitter for passive heat release from enclosures, Sci. Adv. 6 (2020) eabb1906.
[40] C. Lin, Y. Li, C. Chi, Y.S. Kwon, J. Huang, Z. Wu, J. Zheng, G. Liu, C.Y. Tso, C. Y. Chao, A solution-processed inorganic emitter with high spectral selectivity for efficient subambient radiative cooling in hot humid climates, Adv. Mater. 34 (2022) 2109350.
[41] K. Tang, K. Dong, J. Li, M.P. Gordon, F.G. Reichertz, H. Kim, Y. Rho, Q. Wang, C.-Y. Lin, C.P. Grigoropoulos, Temperature-adaptive radiative coating for all-season household thermal regulation, Science 374 (2021) 1504–1509.
[42] G. Jacucci, L. Schertel, Y. Zhang, H. Yang, S. Vignolini, Light management with natural materials: from whiteness to transparency, Adv. Mater. 33 (2021) 2001215.
[43] N.N. Shi, C.-C. Tsai, F. Camino, G.D. Bernard, N. Yu, R. Wehner, Keeping cool: Enhanced optical reflection and radiative heat dissipation in Saharan silver ants, Science 349 (2015) 298–301.
[44] S. Jeong, C.Y. Tso, Y.M. Wong, C.Y. Chao, B. Huang, Daytime passive radiative cooling by ultra emissive bio-inspired polymeric surface, Sol. Energy Mater. Sol. Cells 206 (2020) 110296.

[45] J. Yang, X. Zhang, X. Zhang, L. Wang, W. Feng, Q. Li, Beyond the visible: bioinspired infrared adaptive materials, Adv. Mater. 33 (2021) 2004754.
[46] C. Cai, W. Chen, Z. Wei, C. Ding, B. Sun, C. Gerhard, Y. Fu, K. Zhang, Bioinspired "Aerogel Grating" with Metasurfaces for Durable Daytime Radiative Cooling for Year-round Energy Savings, Nano Energy 108625 (2023).
[47] Z. Cheng, H. Han, F. Wang, Y. Yan, X. Shi, H. Liang, X. Zhang, Y. Shuai, Efficient radiative cooling coating with biomimetic human skin wrinkle structure, Nano Energy 89 (2021) 106377.
[48] J. Mandal, Y. Fu, A.C. Overvig, M. Jia, K. Sun, N.N. Shi, H. Zhou, X. Xiao, N. Yu, Y. Yang, Hierarchically porous polymer coatings for highly efficient passive daytime radiative cooling, Science 362 (2018) 315–319.
[49] T. Wang, Y. Wu, L. Shi, X. Hu, M. Chen, L. Wu, A structural polymer for highly efficient all-day passive radiative cooling, Nat. Commun. 12 (2021) 365.
[50] M.M. Hossain, M. Gu, Radiative cooling: principles, progress, and potentials, Adv. Sci. 3 (2016) 1500360.
[51] H. Zhao, Q. Sun, J. Zhou, X. Deng, J. Cui, Switchable cavitation in silicone coatings for energy-saving cooling and heating, Adv. Mater. 32 (2020) 2000870.
[52] K. Bu, X. Huang, X. Li, H. Bao, Consistent Assessment of the Cooling Performance of Radiative Cooling Materials, Adv. Funct. Mater. (2023) 2307191.
[53] A. Aili, Z. Wei, Y. Chen, D. Zhao, R. Yang, X. Yin, Selection of polymers with functional groups for daytime radiative cooling, Mater. Today Phys. 10 (2019) 100127.
[54] E. Lepeltier, C. Bourgaux, P. Couvreur, Nanoprecipitation and the "Ouzo effect": Application to drug delivery devices, Adv. Drug Deliv. Rev. 71 (2014) 86–97.
[55] S.A. Vitale, J.L. Katz, Liquid droplet dispersions formed by homogeneous liquid–liquid nucleation:"The ouzo effect", Langmuir 19 (2003) 4105–4110.
[56] S.-J. Chiu, S.-Y. Wang, H.-C. Chou, Y.-L. Liu, T.-M. Hu, Versatile synthesis of thiol- and amine-bifunctionalized silica nanoparticles based on the ouzo effect, Langmuir 30 (2014) 7676–7686.
[57] H. Kempe, M. Kempe, Ouzo polymerization: A bottom-up green synthesis of polymer nanoparticles by free-radical polymerization of monomers spontaneously nucleated by the Ouzo effect; Application to molecular imprinting, J. Colloid. Interf. Sci. 616 (2022) 560–570.